magnetochemistry

MDPI

Article

Controlled Synthesis, Microstructure Evolution, and Soft Magnetic Properties of Flaky Iron Nitride

Sicheng Zhai, Xiaoqiang Li, Changkuan Zheng and Qun Wang *

Institute of Materials Science and Engineering, Beijing University of Technology, Beijing 100124, China; zscshr123321@163.com (S.Z.)

* Correspondence: wangq@bjut.edu.cn

Abstract

Ball milling treatment facilitates the transformation of carbonyl iron powders from a spherical to a flaky morphology, while simultaneously introducing numerous defects that approach the nanometer scale in one dimension. Flaky iron nitride was synthesized via the gas nitridation in an NH_3/N_2 atmosphere. The microstructure, morphology, and magnetic properties of the samples nitrided at different temperatures were characterized using XRD, SEM, TEM, and VSM. The formation of γ'-Fe_4N and ε-Fe_3N phases impedes domain wall movement, resulting in a slight increase in the H_c of the samples. Notably, γ'-Fe_4N positively influences the magnetic properties of iron nitride. As the nitriding temperature rises, the content of the γ'-Fe_4N phase initially increases before subsequently declining. Consequently, the flaky iron nitride synthesized at 610 °C exhibits excellent soft magnetic properties with a high M_s value reaching up to 177.1 emu/g and a low H_c value, indicating its potential applications in the field of magnetic materials.

Keywords: flaky iron nitride; microstructures; magnetic properties; nitriding temperature

1. Introduction

Iron nitride, a representative of transition metal nitrides, possesses a diverse array of applications in magnetic and electromagnetic devices, as well as in areas requiring high wear and corrosion resistance, catalysis, and electromagnetic wave absorption [1–4]. Based on nitrogen content, iron nitrides can be classified into several phases, including ξ-Fe_2N, ε-Fe_3N, γ'-Fe_4N, and α''-$Fe_{16}N_2$. Each phase of iron nitride displays distinct physical and chemical properties [5–7]. Notably, γ'-Fe_4N has emerged as a focal point of research within the domain of soft magnetic materials, owing to its advantageous characteristics, which encompass excellent chemical stability, oxidation resistance, outstanding soft magnetic properties, and commendable wear resistance [8–10]. However, the preparation of single-phase γ'-Fe_4N presents considerable challenges, as the presence of the ε-Fe_3N phase and incomplete nitrided precursors may occur. This difficulty can be attributed to the relatively limited stable nitrogen content and temperature range indicated by the phase diagram of iron nitride [11,12]. Consequently, numerous researchers are focused on the synthesis of single-phase γ'-Fe_4N or iron nitride composites with a high proportion of γ'-Fe_4N. The primary method employed for the preparation of iron nitride involves ammonia decomposition followed by nitriding [13].

Fe-Fe_4N spherical particles were synthesized by gas-atomized α-Fe powders with an average diameter of 30 μm in an NH_3/H_2 atmosphere, demonstrating excellent soft magnetic properties [14]. Elemental Fe was produced by reducing the Fe_2O_3 precursor

Check for updates

Academic Editor: Carlos J. Gómez García

Received: 19 November 2025
Revised: 17 December 2025
Accepted: 19 December 2025
Published: 23 December 2025

Copyright: © 2025 by the authors. Licensee MDPI, Basel, Switzerland. This article is an open access article distributed under the terms and conditions of the Creative Commons Attribution (CC BY) license.

in an H_2 atmosphere. Subsequently, the γ′-Fe_4N nanoparticles underwent nitridation at elevated temperatures in an NH_3/H_2 atmosphere, resulting in a magnetic saturation (M_s) that is more than three times greater than that of Fe_2O_3 [15]. Presently, most studies primarily concentrate on spherical particles, with relatively few investigations exploring morphological diversity. Flake-like hexagon α-Fe_2O_3 was synthesized via a chemical process, followed by nitridation to produce porous flaky γ′-Fe_4N@Fe oxide particles. Nevertheless, the preparation procedure for the flaky precursors proved to be relatively complex [16]. The α-Fe_2O_3 precursor prepared via the solvothermal method was subjected to high-temperature nitriding treatment under nitrogen protection to obtain iron nitride, which exhibits favorable soft magnetic properties with a high M_s value reaching up to 163 emu/g [17]. A series of iron nitride thin films was fabricated on silicon substrates using reactive RF magnetron sputtering in a N_2-Ar atmosphere [18]. In contrast to powder forms, thin film materials encounter challenges in large-scale production and subsequent applications of iron nitride [19]. The flaky porous γ′-Fe_4N@SiO_2 particles were synthesized by nitriding Fe_2O_3@SiO_2 which was produced through hydrothermal synthesis and sol–gel coating treatment. The electromagnetic properties were examined in the frequency range of 2–18 GHz, revealing significant potential for applications in the field of microwave absorption [20].

In this study, flaky carbonyl iron powders were prepared through a ball milling treatment, subsequently followed by the synthesis of flaky iron nitride via the gas nitriding method. This approach enabled the morphological diversity of iron nitride to satisfy various application requirements. The effects of nitriding temperatures on the microstructure, morphology, and magnetic properties of flaky iron nitride have been systematically investigated, aiming to yield iron nitride with excellent soft magnetic properties and to enhance the application of soft magnetic materials.

2. Experimental Procedures

Carbonyl iron powders (99.5% purity, Runzhijiabo Metal Materials Co., LTD, Beijing, China) with an average particle size of 3–5 μm were subjected to ball milling in a sand mill (HWSM-0.4-II, Shanghai Hewei Electromechanical Equipment Co., LTD, Shanghai, China) for different durations of 1 h, 2 h, and 4 h. This process employed ZrO_2 balls with an average particle size of 1 mm to facilitate the transformation of the spherical particles into flaky forms and to refine the grain structure. Following this, the carbonyl iron powders milled for 4 h were placed in a boat, which was then positioned at the center of a tubular furnace for the nitriding process. The nitrided powders were synthesized by nitriding in an NH_3 and N_2 atmosphere at a gas flow rate of 400 Sccm, with nitriding temperatures set at 590 °C, 610 °C, and 630 °C for 1 h. Upon the completion of the nitriding process, the samples were cooled to room temperature in an N_2 atmosphere to obtain the iron nitride powders.

The crystal structures of carbonyl iron powders subjected to different milling durations, as well as nitrided powders synthesized at various nitriding temperatures, were characterized using X-ray diffraction (XRD, Rigaku D8 Advance, Bruker AXS, Karlsruhe, Germany) with Cu Kα radiation (λ = 0.15406 nm), scanning an angle range from 20 to 100°. The surface morphologies of the carbonyl iron powders with different milling durations were examined using a field emission scanning electron microscope (FESEM, GeminiSEM 300, ZEISS, Oberkochen, Germany). Furthermore, the microstructure of the carbonyl iron powders milled for 4 h was further characterized using transmission electron microscopy (TEM, Talos F200S, FEI, Hillsboro, OR, USA) coupled with selected area electron diffraction (SAED) and high-resolution transmission electron microscopy (HRTEM). The magnetic properties were measured at room temperature using a vibrating sample magne-

tometer (VSM, 7404, LakeShore, Westerville, OH, USA) with a maximum applied field of ±20,000 Oe.

3. Results and Discussion

Figure 1 illustrates the XRD patterns of carbonyl iron powders subjected to ball milling for different durations. In comparison with the JCPDS standard card, the characteristic diffraction peaks at 2θ = 44.7°, 65.0°, 82.3°, and 98.9° correspond to the (110), (200), (211), and (222) crystal planes of the α-Fe phase (PDF# 87-0722), which exhibits a bcc structure. However, a minor deviation of approximately 0.1° is observed in the characteristic peaks associated with α-Fe, as determined by Gauss fitting using Origin software, 2025b, which may be attributed to errors inherent in the XRD testing. Importantly, no significant structural alterations are observed in the carbonyl iron powders following ball milling for different durations. The full width at half maximum (FWHM) fitting of the XRD curves reveals that as the duration of ball milling increases, the FWHM values also increase, indicating a refinement of the grains in the ball-milled samples.

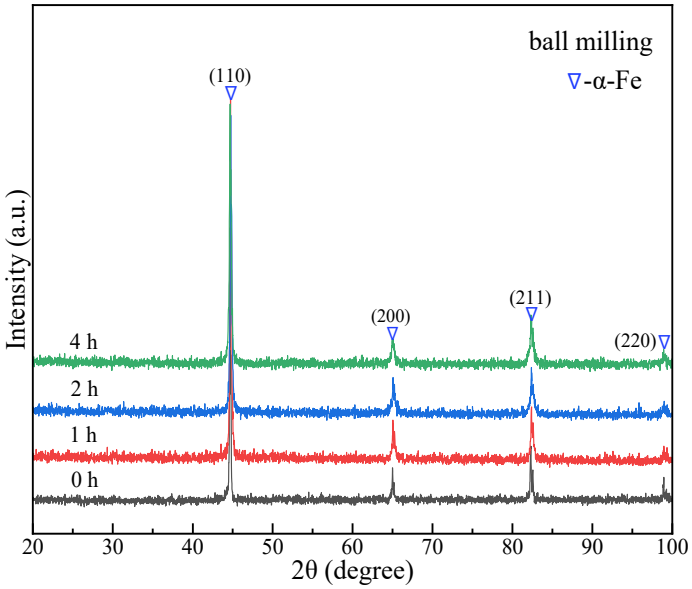


Figure 1. XRD patterns of the carbonyl iron powders with different milling durations.

Figure 2 presents the SEM images that illustrate the morphological evolution of carbonyl iron powders subjected to varying durations of ball milling. In comparison to the untreated carbonyl iron powders, the ball milling process significantly altered the morphology, resulting in the ball-milled carbonyl iron powders exhibiting a range of morphologies and geometric shapes. Notably, the carbonyl iron powders subjected to ball milling progressively transition from a smooth spherical form to a flaky structure. Moreover, as the duration of ball milling increases, the extent of this transformation also increases. Nevertheless, a limited number of spherical particles remain that have not fully converted into flaky forms. Additionally, the SEM images reveal that the carbonyl iron powders experienced a nanoscale transformation at a one-dimensional scale during the ball milling process.

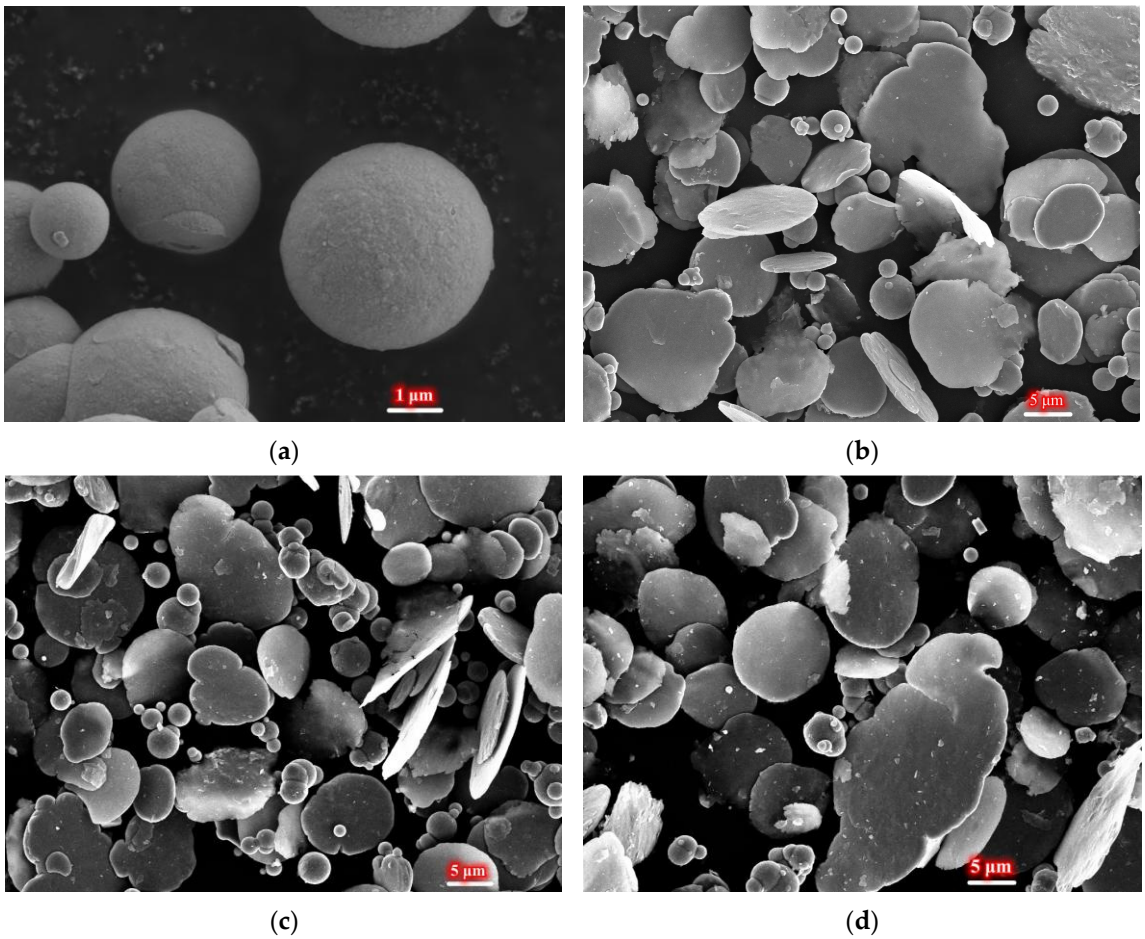


Figure 2. FESEM images of the carbonyl iron powders with different milling durations: (**a**) 0 h; (**b**) 1 h; (**c**) 2 h; (**d**) 4 h.

To further explore the effects of varying milling durations on the microstructures of carbonyl iron powders, a sample milled for 4 h was examined using TEM/HRTEM coupled with SAED patterns, as shown in Figure 3. As illustrated in Figure 3a, no discernible second phase is evident in the carbonyl iron powders following ball milling. The corresponding SAED pattern reveals that the diffraction rings of the BCC structure correspond to the (110), (200), and (211) crystal planes of α-Fe, as depicted in Figure 3c. The lattice fringes calculated from the HRTEM images in Figure 3b measure approximately 0.21 nm, corresponding to the (110) crystal plane of α-Fe phase [21]. Notably, the dislocation defects and stacking faults are observed in the HRTEM images (marked by rings), suggesting that the ball milling process promotes a tendency towards flaky transformation within the carbonyl iron powders while simultaneously introducing additional defects that may enhance the nitriding process.

The magnetic hysteresis loops (M-H) of carbonyl iron powders subjected to ball milling for different durations at room temperature are depicted in Figure 4. The enlarged local view in Figure 4 allows for a clearer observation of the coercivity (H_c) values for the milled samples. All M-H curves display sigmoidal hysteresis loops without any humps, indicating characteristic soft magnetic behavior. Notably, the milled samples demonstrate a high M_s value, indicating the excellent soft magnetic properties. The effects of ball milling on the M_s and H_c values of the carbonyl iron powders are illustrated in Figure 5.

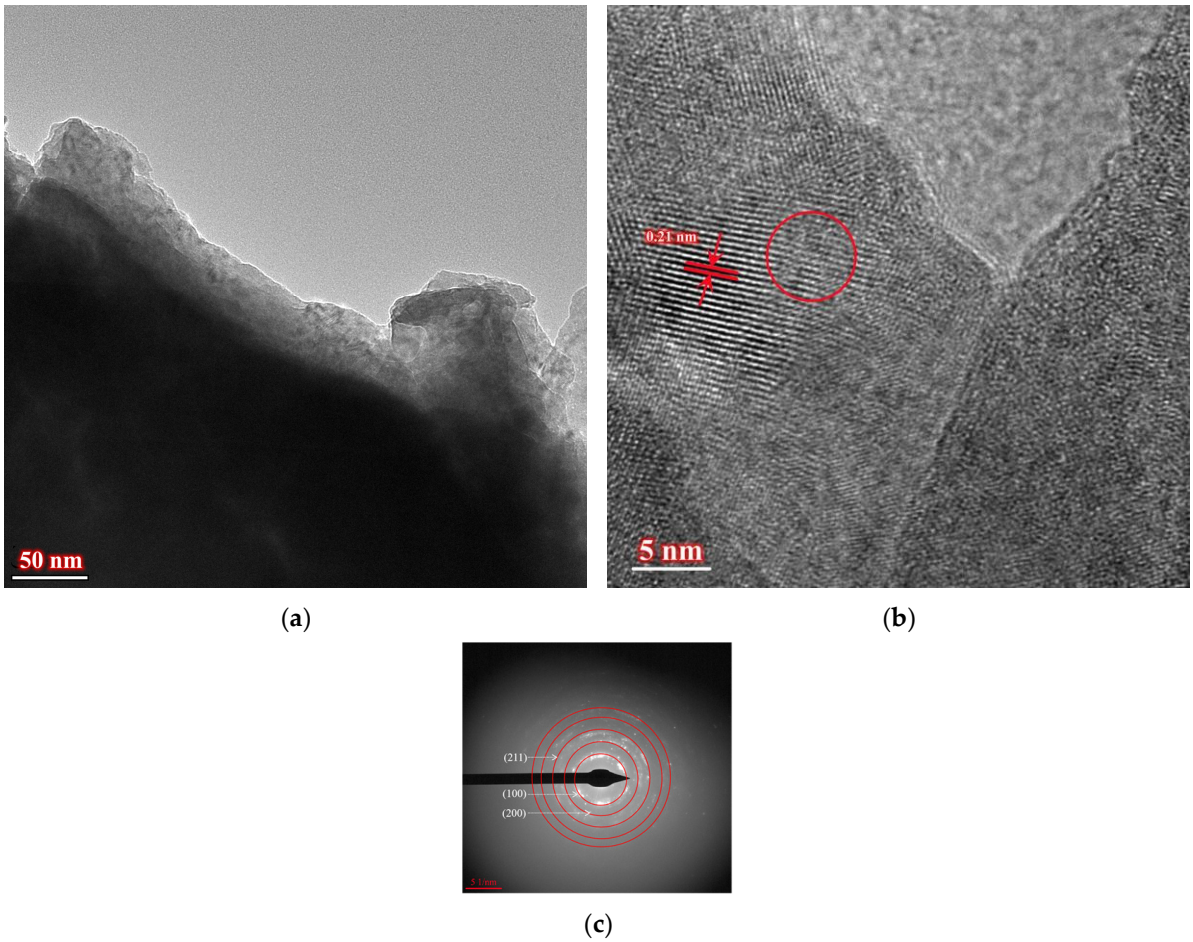


Figure 3. Bright-field TEM (**a**), HRTEM (**b**) images, and the SARD pattern (**c**) corresponding to (**a**) of the carbonyl iron powders after 4 h milling duration.

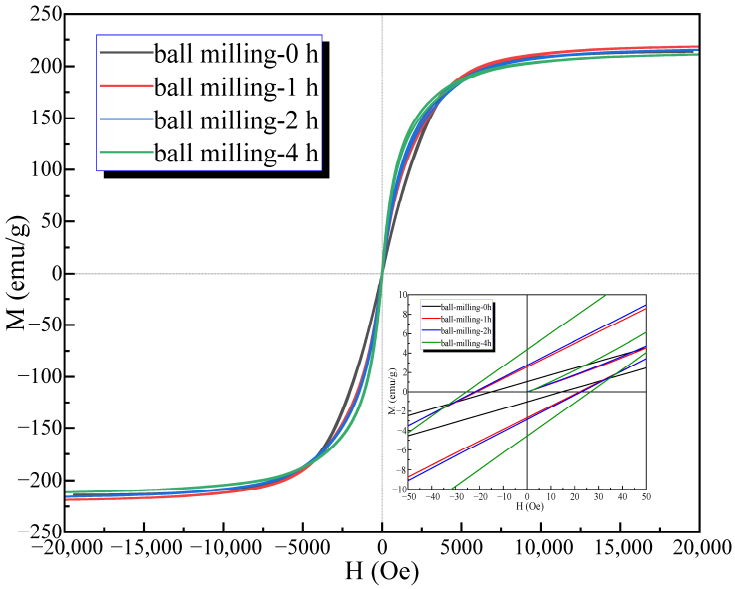


Figure 4. Magnetic hysteresis loops of the carbonyl iron powders with different milling durations.

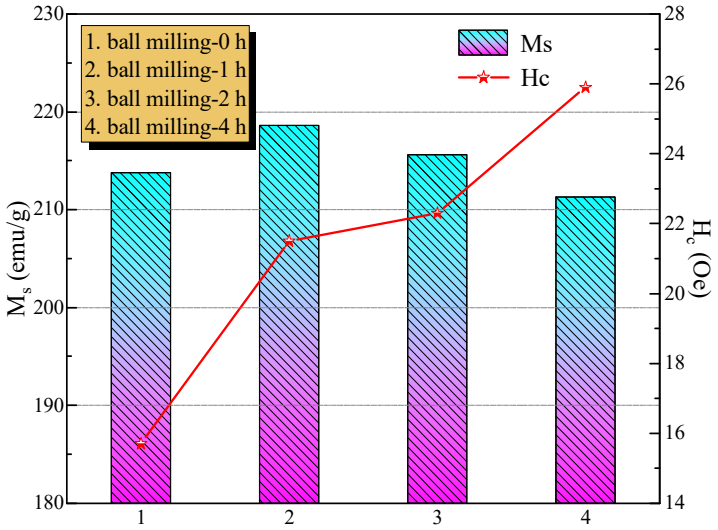


Figure 5. The corresponding H_c and M_s values of carbonyl iron powders with different milling durations. (The lines of H_c values are drawn as guides to the eyes).

Figure 5 illustrates that as the nitriding duration is extended, the M_s value of the ball-milled carbonyl iron powders initially increases before subsequently decreasing. This phenomenon can be attributed to the collisions between ZrO_2 and the carbonyl iron powders, which cause the oxide layer on the surface of the carbonyl iron powders to detach, thereby increasing the M_s value. However, with prolonged milling duration, these collisions become more pronounced, disrupting the ordered arrangement of magnetic moments and resulting in a decrease in the M_s value. In comparison to the H_c value of carbonyl iron powders, the H_c values of the flaky samples following ball milling exhibited a slight increase. This can be attributed to the ball milling process introducing internal defects into the samples, which serve as pinning sites and impede the movement of magnetic domain walls [22]. Consequently, the ball milling treatment adversely influences the H_c value of the samples.

The XRD patterns of the iron nitride powders obtained after 4 h of ball milling at different nitriding temperatures are presented in Figure 6. The diffraction peaks at 2θ = 41.2°, 47.9°, 70.1°, 84.6°, and 89.4° correspond to the (111), (200), (220), (311), and (222) crystal planes of the γ′-Fe_4N (PDF# 83-0875) phase, respectively [23]. Furthermore, the diffraction peaks at 2θ = 38.1°, 43.4°, 57°, 69.2°, 76.8° and 83.8° correspond to the (110), (111), (112), (300), (113) and (302) crystal planes of ε-Fe_3N (PDF# 83-0877), respectively, which is consistent with previous reports [24]. It is evident that the synthesized nitride products comprise γ′-Fe_4N and ε-Fe_3N, a result of the introduction of additional defects during the ball milling process. These defects, which include layer faults and grain boundaries, facilitate the diffusion of active nitrogen atoms.

The nitriding process can be divided into two distinct steps: the decomposition of NH_3 and the diffusion of active nitrogen atoms within Fe [25].

$$\begin{aligned} &NH_3 \underset{500\sim700°C}{\overset{Fe}{\rightarrow}} \tfrac{3}{2}H_2 + [N] \\ &4Fe + [N] \rightarrow Fe_4N \\ &3Fe + [N] \rightarrow Fe_3N \end{aligned} \quad (1)$$

The areas of the diffraction peaks of γ′-Fe_4N and ε-Fe_3N phases were fitted to obtain the relative contents using the Jade 6 software. As the nitriding temperature increases, the content of the γ′-Fe_4N phase of nitrided samples at different temperatures initially rises before subsequently declining, with corresponding values of 85.7%, 87.2%, and 84.3%,

respectively. It has been reported that as the nitriding temperature increases, the carbonyl iron powders gradually transform into γ′-Fe_4N. With the continued diffusion of active nitrogen atoms, γ′-Fe_4N further converts into ε-Fe_3N. Subsequently, a portion of the ε-Fe_3N phase decomposes and reverts back to γ′-Fe_4N [26,27].

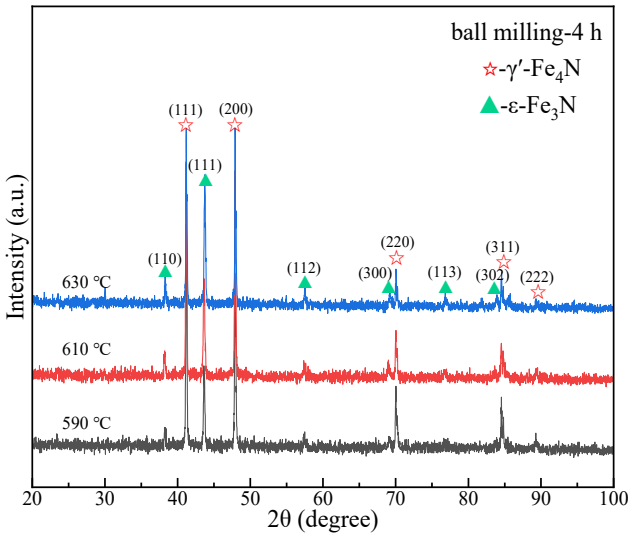


Figure 6. XRD patterns of the iron nitride powders at different nitriding temperatures after 4 h milling duration.

To further confirm the morphology and distribution of the powders following nitriding, the SEM image of the iron nitride powders nitrided at 590 °C is presented in Figure 7. It is evident that the iron nitride retains a flaky powder morphology following nitriding. In comparison to the carbonyl iron powders produced after ball milling, the iron nitride powders demonstrate a more pronounced agglomeration phenomenon.

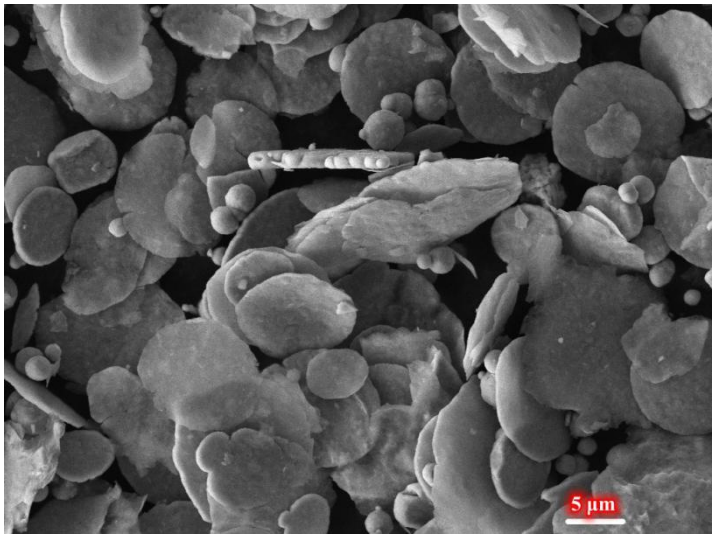


Figure 7. FESEM image of the flaky iron nitride at a 590 °C nitriding temperature.

The room temperature magnetic hysteresis loops of the flaky iron nitride powders synthesized at different nitriding temperatures are depicted in Figure 8. The magnified local view in the illustration facilitates the observation of the H_c values for the nitrided samples synthesized at different nitriding temperatures. All the M-H curves display the sigmoidal hysteresis loops without any humps, indicating the characteristic soft magnetic behavior.

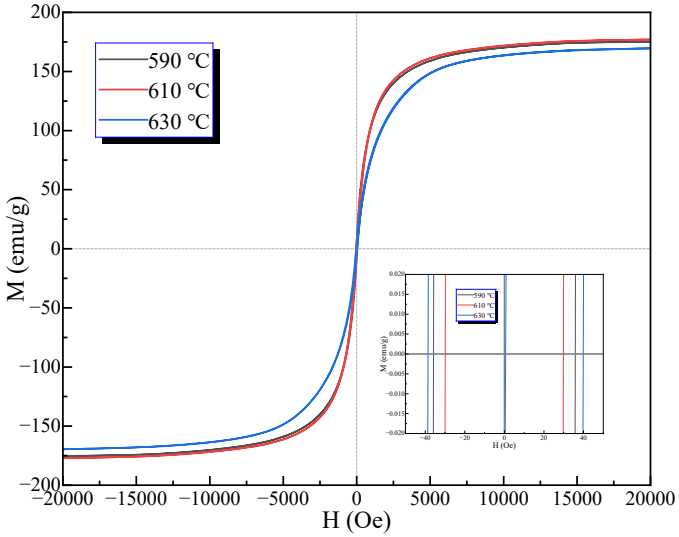


Figure 8. Magnetic hysteresis loops of the flaky iron nitride after 4 h milling and nitriding at different nitriding temperatures.

The effects of nitriding temperatures on the M_s and H_c values of the iron nitride are illustrated in Figure 9. In contrast to flaky carbonyl iron powders, the H_c of iron nitride is increased, which can be attributed to the precipitation of the γ′-Fe_4N and ε-Fe_3N phases that enhance magnetic anisotropy [28]. Furthermore, these phases can act as quasi-dislocation dipoles (QDD), thereby increasing the density of pinning sites for domain wall movement [29]. An analysis of the phase content derived from the XRD patterns reveals that as the content of ε-Fe_3N increases, the H_c of iron nitride also rises, suggesting that ε-Fe_3N adversely affects the magnetic properties of the material. It is noteworthy that γ′-Fe_4N exerts a positive influence on the magnetic properties of the material. In comparison to the ε-Fe_3N phase, γ′-Fe_4N exhibits a higher theoretical M_s value of 208 emu/g [30]. Consequently, the iron nitride, which contains a high proportion of γ′-Fe_4N and is synthesized through nitriding at 610 °C, presents a higher M_s (177.1 emu/g) and a lower H_c, exceeding the magnetic properties of previously reported iron nitride and other soft magnetic materials [31,32].

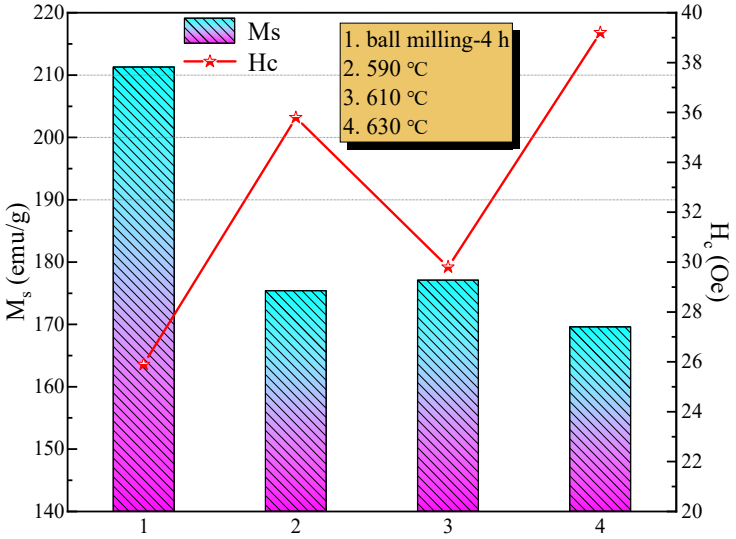


Figure 9. The corresponding H_c and M_s values of the flaky iron nitride after 4 h milling and nitriding at different nitriding temperatures.

https://doi.org/10.3390/magnetochemistry12010003

4. Conclusions

In this study, flaky iron nitride was successfully synthesized via gas nitridation in an NH_3/N_2 atmosphere. The effects of nitriding temperatures on the microstructure and soft magnetic properties of flaky iron nitride have been investigated. The treatment of carbonyl iron powders via ball milling results in a transformation to a flaky morphology. As the duration of ball milling increases, the degree of flake formation intensifies, leading to a tendency towards nanoscale dimensions in one dimension and the introduction of numerous defects. The flaky γ'-Fe_4N/ε-Fe_3N composite, characterized by a high content of γ'-Fe_4N (87.2%), synthesized by nitriding at 610 °C, presents excellent soft magnetic properties, with the highest M_s up to 177.1 emu/g, indicating promising application potential in the field of magnetic materials.

Author Contributions: S.Z.: Writing—original draft, Methodology, Investigation, Data curation. Q.W.: Writing—review and editing, Supervision, Conceptualization. X.L.: Writing—review and editing, Supervision, Conceptualization. C.Z.: Writing—review and editing, Supervision, Conceptualization. All authors have read and agreed to the published version of the manuscript.

Funding: This research was funded by [National Key Research Program] grant number [2016YFB1200602-37] And The APC was funded by [National Key Research Program], grant No. 2016YFB1200602-37.

Institutional Review Board Statement: Not applicable.

Informed Consent Statement: Not applicable.

Data Availability Statement: The original contributions presented in this study are included in the article. Further inquiries can be directed to the corresponding author.

Conflicts of Interest: The authors declare no conflicts of interest.

References

1. Li, X.; Wang, Q.; Yu, Y.; Zhai, S. Optimizing the electromagnetic wave absorption properties of core-shell Fe/FeN/Fe_3C@GN nanoparticles by low-temperature NH_3 plasma. *Carbon* **2024**, *226*, 119237. [CrossRef]
2. Chang, X.; Liu, S.; Huang, T.; Yan, Z.; Zhao, Y.; Tong, W.; Wang, J. Study on intermediate annealing-twice nitriding process and corrosionresistance of pure iron. *Mater. Charact.* **2025**, *229*, 115631. [CrossRef]
3. Zhuo, S.N.; Sun, H.; Wang, Z.Y.; Ren, H.Y.; Xing, D.F.; Ren, N.Q.; Liu, B.F. A magnetic biochar catalyst with dual active sites of Fe_3C and Fe_4N derived from floc: The activation mechanism for persulfate on degrading organic pollutant. *Chem. Eng. J.* **2023**, *455*, 140702. [CrossRef]
4. Huang, H.; Shang, X.; Wang, Q.; Cao, M.; Sun, F.; Liu, W.; Xu, Y.; Wang, J.; Zhao, Y.; Ma, X. Epsilon iron carbide derived from Fe4N for ethanol synthesis via esterhydrogenation. *J. Energy Chem.* **2025**, *108*, 19–29. [CrossRef]
5. Bhattacharyya, S. Iron nitride family at reduced dimensions: A review of their synthesis protocols and structural and magnetic properties. *J. Phys. Chem. C* **2015**, *119*, 1601–1622. [CrossRef]
6. Zhao, Z.; Li, Z.; Shen, X. Structures, magnetic and electronic properties of Fe2N adsorbed andinserted capped single-walled carbon nanotubes. *Mater. Chem. Phys.* **2021**, *260*, 124098. [CrossRef]
7. Kikkawa, S.; Masubuchi, Y.J. Magnetic iron nitrides inspired by historic research on a''-$Fe_{16}N_2$. *Prog. Solid State Chem.* **2018**, *51*, 19–26. [CrossRef]
8. Leineweber, A.; Hickel, T.; Azimi-Manavi, B.; Maisel, S.B. Crystal structures of Fe_4C vs. Fe_4N analysed by DFT calculations: Fcc-based interstitial superstructures explored. *Acta Mater.* **2017**, *140*, 433–442.
9. Zhang, S.; Meng, X.; Wang, C.; Yu, M. Design and synthesis of Fe_4N/MnO/carbon nanofibers for efficientelectromagnetic wave absorption. *Chem. Eng. J.* **2025**, *524*, 169749.
10. Yin, H.; Zhang, C.Z.; Liu, F.; Hou, Y.L. Hybrid of Iron Nitride and Nitrogen-Doped Graphene Aerogel as Synergistic Catalyst for Oxygen Reduction Reaction. *Adv. Funct. Mater.* **2014**, *24*, 2930–2937. [CrossRef]
11. du Marchie van Voorthuysen, E.H.; Chechenin, N.C.; Boerma, D.O. Low-temperature extension of the lehrer diagram and the iron-nitrogen phase diagram. *Metall. Mater. Trans. A* **2002**, *33*, 2593–2598. [CrossRef]
12. Zieschang, A.M.; Bocarsly, J.D.; Dürrschnabel, M.; Molina-Luna, L.; Kleebe, H.J.; Seshadri, R.; Albert, B. Nanoscale Iron Nitride, ε-Fe_3N: Preparation from Liquid Ammonia and Magnetic Properties. *Chem. Mater.* **2017**, *29*, 621–628.

13. Yamaguchi, T.; Sakita, M.; Nakamura, M.; Kobira, T. Synthesis and characteristics of Fe_4N powders and thin films. *J. Magn. Magn. Mater.* **2000**, *215*, 529–531. [CrossRef]
14. Peng, X.; Yu, S.; Chang, J.; Ge, M.; Li, J.; Ellis, T.; Yang, Y.; Xu, J.; Hong, B.; Jin, D.; et al. Preparation and magnetic properties of Fe_4N/Fe soft magnetic composites fabricated by gas nitridation. *J. Magn. Magn. Mater.* **2020**, *500*, 166407. [CrossRef]
15. Wu, K.; Liu, J.; Saha, R.; Ma, B.; Su, D.; Peng, C.; Sun, J.; Wang, J.P. Irregularly Shaped Iron Nitride Nanoparticles as a Potential Candidate for Biomedical Applications: From Synthesis to Characterization. *ACS Omega* **2020**, *5*, 11756−11767. [CrossRef]
16. Zheng, Q.; Yu, M.; Wang, W.; Liu, S.; Liang, X.; Wang, C.; Dai, Y.; Xu, Y. Porous and flake-like γ′-Fe_4N@iron oxides with enhanced microwave absorption performance. *Ceram. Int.* **2021**, *47*, 8315–8321. [CrossRef]
17. Liu, Y.; Qie, Y.; Kong, F.; Yang, Z.; Yang, H. Synthesis and magnetism of single-phase γ′-Fe_4N by non-ammonia route and applied in oxygen evolution reaction electrocatalysis. *Mater. Today Commun.* **2022**, *30*, 103103.
18. Li, X.; Sun, X.; Wang, J.; Liu, Q. Microstructure and magnetic properties of iron nitride thin films. *J. Alloys Compd.* **2014**, *582*, 398–402. [CrossRef]
19. Lu, Q.H.; Xie, M.L.; Han, G.L.; Zheng, B.; Song, Y.Z.; Qiang, J.; Wang, X.Q.; Wu, Z.G.; Yan, P.X.; Liu, W.M. Controllable synthesis of γ′-Fe_4N via prolonged high vacuum magnetic annealing of deposited Fe-N thin films. *J. Magn. Magn. Mater.* **2019**, *474*, 76–82.
20. Liu, S.; Yu, M.; Zheng, Q.; Liang, X.; Xie, S.; Xu, Y.; Wang, C. Optimized impedance matching and enhanced microwave absorbing performance of porous flaky Fe_4N wrapped with SiO_2. *J. Magn. Magn. Mater.* **2021**, *536*, 168119. [CrossRef]
21. Tan, X.; Wang, S.; Chen, Y.; Zhou, Y.; Li, Z. Design, preparation and characterization of iron nitride magnetic abrasives. *J. Alloys Compd.* **2019**, *774*, 443–450.
22. Li, J.; Estévez, D.; Jiang, K.; Yang, W.; Man, Q.; Chang, C.; Wang, X. Electronic-structure origin of the glass-forming ability and magnetic properties in Fe-RE-B-Nb bulk metallic glasses. *J. Alloys Compd.* **2014**, *617*, 332–336. [CrossRef]
23. Pandey, N.; Gupta, M.; Rawat, R.; Amir, S.; Stahn, J.; Gupta, A. Role of growth parameters on structural and magnetic properties of Fe_4N thin films grown by reactive magnetron sputtering. *Phys. B Condens. Matter* **2019**, *572*, 36–41.
24. Yin, W.; Lei, L.; Jiang, X.; Liu, P.; Liu, F.; Li, Y.; Peng, F.; He, D. High pressure synthesis and properties studies on spherical bulk ε-Fe_3N. *High Press. Res.* **2014**, *34*, 317–326.
25. Arabczyk, W.; Pelka, R. Studies of the Kinetics of Two Parallel Reactions: Ammonia Decomposition and Nitriding of Iron Catalyst. *J. Phys. Chem. A* **2009**, *113*, 411–416. [CrossRef] [PubMed]
26. Kardonina, N.; Yurovskikh, A.; Kolpakov, A. Transformations in the Fe-N System. *Met. Sci. Heat Treat.* **2010**, *52*, 457–467. [CrossRef]
27. Wróbel, R.; Arabczyk, W. Solid-Gas Reaction with Adsorption as the Rate Limiting Step. *J. Phys. Chem. A* **2006**, *110*, 9219–9224. [CrossRef]
28. Kronmüller, H. Theory of magnetic after-effects in ferromagnetic amorphous alloys. *Philos. Mag. B Phys. Condens. Matter* **1983**, *48*, 127–150. [CrossRef]
29. Bitoh, T.; Makino, A.; Inoue, A. Quasi-Dislocation Dipole-Type Defects and Low Coercivity of Fe-Based Soft Magnetic Glassy Alloys. *J. Metastable Nanocryst. Mater.* **2005**, *24*, 427–430. [CrossRef]
30. Wang, C.; Jin, X.; Li, T.; Jia, Z.; Xue, D. High performance in soft magnetic composites of Fe-Fe_4N particles. *J. Magn. Magn. Mater.* **2024**, *605*, 172336. [CrossRef]
31. Khan, W.; Wang, Q.; Jin, X.; Yasin, G. Corrosion, optical and magnetic properties of flexible iron nitride nano thin films deposited on polymer substrate. *Phys. B* **2017**, *524*, 71–80. [CrossRef]
32. Li, W.; Li, W.; Chen, J.; Ying, Y.; Yu, J.; Zheng, J.; Qiao, L.; Li, J.; Che, S. Migration of N element and evolution of microstructure in spark plasma sintered bulk γ′-Fe_4N. *J. Alloys Compd.* **2022**, *928*, 167201. [CrossRef]

Disclaimer/Publisher's Note: The statements, opinions and data contained in all publications are solely those of the individual author(s) and contributor(s) and not of MDPI and/or the editor(s). MDPI and/or the editor(s) disclaim responsibility for any injury to people or property resulting from any ideas, methods, instructions or products referred to in the content.